MATERIALS SCIENCE

Physics-guided co-designing flexible thermoelectrics with techno-economic sustainability for low-grade heat harvesting

Yi Zhou[1,2], Xixi Liu[3], Baohai Jia[1], Tianpeng Ding[2], Dasha Mao[1], Tiancheng Wang[1], Ghim Wei Ho[2,4,5]*, Jiaqing He[1,6,7]*

Flexible thermoelectric harvesting of omnipresent spatial thermodynamic energy, though promising in low-grade waste heat recovery (<100°C), is still far from industrialization because of its unequivocal cost-ineffectiveness caused by low thermoelectric efficiency and power-cost coupled device topology. Here, we demonstrate unconventional upcycling of low-grade heat via physics-guided rationalized flexible thermoelectrics, without increasing total heat input or tailoring material properties, into electricity with a power-cost ratio (W/US$) enhancement of 25.3% compared to conventional counterparts. The reduced material usage (44%) contributes to device power-cost "decoupling," leading to geometry-dependent optimal electrical matching for output maximization. This offers an energy consumption reduction (19.3%), electricity savings (0.24 kWh W^{-1}), and CO_2 emission reduction (0.17 kg W^{-1}) for large-scale industrial production, fundamentally reshaping the R&D route of flexible thermoelectrics for techno-economic sustainable heat harvesting. Our findings highlight a facile yet cost-effective strategy not only for low-grade heat harvesting but also for electronic co-design in heat management/recovery frontiers.

INTRODUCTION

Converting low-grade heat (<100°C) from the surroundings into electricity plays a crucial role in alleviating the energy crisis and global warming, especially for the postpandemic sustainable development as the economic activity gradually recovers with ever-increasing energy demand (expected to increase by 4%) (*1*–*3*). In this context, scavenging all-present low-grade waste heat [accounting for >30% of worldwide primary energy consumption (*1*, *4*)] toward energy sustainability is of great interest. Thermoelectrics (TEs) directly convert spatial heat into electricity via the Seebeck effect, offering a promising solution for environmental waste heat harvesting. Typically, the power conversion efficiency (PCE) of TEs is determined by the dimensionless figure-of-merit (ZT), which is defined as $ZT = S^2\sigma T/\kappa$, where S, σ, κ, and T denote the Seebeck coefficient, electrical conductivity, thermal conductivity, and operational temperature, respectively. However, these properties (S, σ, and κ) are intercoupled to both the carrier concentration (n) and electronic structure (e.g., $S \propto n^{-2/3}$, $\sigma \propto n$; $S \propto m^*$, $\sigma \propto 1/m^*$, where m^* is the effective mass), making the achievement of desirable ZT values or power factors ($PF = S^2\sigma$) challenging. During the past two decades, tremendous efforts have been made to attain a high ZT value (up to 3.1) in high-temperature TE materials [e.g., element doping (*5*–*8*), band structure manipulation (*9*, *10*), and nanostructures (*11*, *12*)], and the number of yearly publications exceeds 1000 (fig. S1A). Unfortunately, the average ZT of room temperature TEs (e.g., Bi_2Te_3, Mg_3Sb_2, and conductive polymers) is still less than 1.0 (*13*–*15*), and PCE across a wide temperature range is below 5% (*16*, *17*), especially for <100°C waste heat recovery.

In terms of body heat harvesting or environmental waste heat scavenging, there is only a 5°C attainable temperature gradient (ΔT) due to inevitable heat dissipation or convection, and thus, a PCE of barely 0.25% can be achieved (*18*–*20*). This means that a well-matched thermal interface (negligible thermal contact resistance) between the nonplanar heat source/sink and TE module is critical for maximizing the out-of-plane ΔT and power output. Accordingly, flexible TEs (f-TEs) have been sought by chemical doping (*21*–*23*), physical vapor deposition (*24*), free-standing substrates (*25*, *26*), and organic/inorganic hybridization (*27*–*29*). However, the issue of relatively low PCEs at room temperature still prevails, suggesting that much of the current research focused on the strategy of continuously increasing the peak ZT is not cost-effective for ubiquitous, unusable, low-grade waste heat harvesting toward affordable and clean energy supply (*18*, *30*–*32*). In other words, the concerns related to the output power enhancement, material cost reduction, and power-cost ratio (PCR) increase of f-TE devices for industry-oriented deployment via topology co-design could be equally important as those of ZT and PCE; however, they have been largely overlooked until now (fig. S1) (*33*–*37*). Meanwhile, the geometry of TE legs, correlated thermal conductance, and electrical resistance (R_{te}) are acknowledged to substantially affect the output power and cost-effectiveness (fig. S2A). Consequently, there remain some outstanding challenges regarding f-TE devices for sustainable low-grade heat harvesting: (i) superior flexibility in high-performance room temperature TEs; (ii) economic materials or devices as the power density increases; and (iii)

[1]Shenzhen Key Laboratory of Thermoelectric Materials, Department of Physics, Southern University of Science and Technology, Shenzhen 518055, China. [2]Department of Electrical and Computer Engineering, National University of Singapore, Singapore 117581, Singapore. [3]Shenzhen Thermo-Electric New Energy Co. Ltd., Shenzhen 518112, China. [4]Department of Materials Science and Engineering, National University of Singapore, Singapore 117575, Singapore. [5]Institute of Materials Research and Engineering, A*STAR (Agency for Science, Technology and Research), Singapore 138632, Singapore. [6]Guangdong-Hong Kong-Macao Joint Laboratory for Photonic-Thermal-Electrical Energy Materials and Devices, Southern University of Science and Technology, Shenzhen 518055, China. [7]Key Laboratory of Energy Conversion and Storage Technologies, Southern University of Science and Technology, Ministry of Education, Shenzhen 518055, China.
*Corresponding author. Email: elehgw@nus.edu.sg (G.W.H.); hejq@sustech.edu.cn (J.H.)

device-level durability, stability, and sustainability for potential industrial implementation.

In this work, we report cost-effective and enhanced-PCR f-TEs via rational co-designed device geometry by deploying theoretical, modeling, and experimental approaches to overcome the above-mentioned impediments for industrial low-grade heat harvesting. Our proposition deviates from the conventional uniform geometry factor (GF = 1.0; fig. S2B) or traditional fill factor increases (dense TE legs for output power multiplication) (table S1) (*9*, *35*, *38*–*48*). The narrowed p-type leg and small GF value (GF < 1.0) of the proposed f-TE device not only leads to reduced material usage and electricity savings for fabrication but also rationalizes the heat flowing across the device and electrical matching to maximize the PCR and achieve sustainable techno-economics. Without consuming additional thermal energy, increasing the device fill factor, or tailoring the material properties, the developed f-TE device converts the otherwise unavailable heat (<100°C) into electricity with a relative Carnot efficiency (RCE) of 16.1% and energy savings of 0.24 kWh W^{-1} and remains exceedingly stable after 1000 bending cycles and durability tests. Apart from being facile, the proposed approach is a universal paradigm for realizing cost-effective f-TEs for industry-orientated low-grade heat harvesting. Furthermore, it also provides avenues for the device co-design and integration of other semiconductors/electronics beyond the TE community, e.g., solid-state semiconductor cooling, asymmetric electronics, and thermocells.

RESULTS

The typical TE device fabrication and industrial implementation from ingots/rods to demand-oriented applications are illustrated in Fig. 1. Conventionally, large-scale device fabrication follows an industrialized production process, where an ingot/rod synthesized from raw materials is cut into wafers and further diced into uniform TE legs for mounting and assembly. The consistent dimension of the p- and n-type legs without device geometry design provides a GF value of 1.0. In contrast, our introduced physics-guided co-design aims to rationalize the geometric dimension of TE legs before dicing to achieve cost-effective and sustainable heat harvesting (Fig. 1A). Noticeably, the developed f-TE device with thinner p-type legs (fig. S2B; GF < 1.0) presented high power output, low cost, low weight, well-matched heat transfer, and mechanical stability. The f-TE device was suitable for sustainable industrialization with energy consumption and carbon emission reductions [i.e., to meet the sustainable development goals (SDGs)]. Moreover, according to the TE constitutive equation (fig. S2A; see Materials and Methods for details), the correlation of PCR versus GF and electrical factor (EF) values was revealed and mathematically plotted in Fig. 1B without using any material parameters. Notably, the region of interest (ROI) to achieve a maximized PCR varies with GF values and peaks at 0.6 to 0.9 for known TE materials (EF is unchangeable). These results differ substantially from the conventional design (GF = 1.0, circle dot), suggesting that the co-designed p-type legs (GF < 1.0) enable a power output increase while lowering the material usage for cost-effectiveness enhancement. Furthermore, the state-of-the-art comparison (Fig. 1C and Table 1) of conventional designs and our work evidenced an unprecedented improvement in both the device performance and cost-effectiveness [enhancement of 9.2% in RCE, 12.2% in open-circuit voltage (V_{OC}), 22.4% in maximum specific power (PS_{max}), and 25.3% in the PCR value].

Physical modeling and experimental verification

To elucidate how the GF value affects the electrical output and cost-effectiveness of the f-TE device for waste heat harvesting, as well as the underlying TE characteristics, we performed finite element modeling using the COMSOL Multiphysics software (fig. S3; see Materials and Methods for details). Room temperature commercial bismuth telluride materials ($Bi_{0.4}Sb_{1.6}Te_3$ and $Bi_2Te_{2.85}Se_{0.15}$) with high TE performance were used (fig. S4). The contours of maximum power density (PD_{max}) and PCE_{max} illustrated that the height and GF optimization in the desired power and efficiency were different (Fig. 2, A and B). For instance, a considerable height of the TE leg offered a high PCE, whereas PD_{max} required small height since the impedance ratio of PD_{max} (λ_{P_max}= 1) was less than that of PCE_{max} ($\lambda_{PCE\_max} = \sqrt{1 + ZT_{ave}} > 1$). In other words, the total resistance of a device at PCE_{max} is greater than that at P_{max}, so the dimension-dependent internal resistance of the device at PCE_{max} (R_{PCE_max}) and P_{max} (R_{P_max}) follows $R_{PCE\_max} > R_{P\_max}$, i.e., height-dependent electrical output, for a known invariable R_L (Eqs. 3 and 7; see Materials and Methods for details). However, with a recommended height of 1.78 mm for p- and n-type legs from commercial TE modules, the GF for PD_{max} and PCE_{max} peaked at 0.5 to 0.9 with an overlapped ROI. Specifically, from the viewpoint of GF-dependent output, the resistance of a TE leg is linear to the reciprocal value of the cross-sectional area (A_p or A_n) at a given height (Eq. 8; see Materials and Methods for details). In this context, GF = 1.0 ($A_p = A_n$) offers a low internal resistance and benefits to achieve a high output power (P_O; Fig. 2, C and D), whereas GF = 0.56 ($A_p < A_n$) contributes to obtaining a high PCE and V_{OC}. Thereby, the GF of ~0.56 is a rationalized design for an optimized device with a high PCE and V_{OC} while maintaining a modest output power. Moreover, we fabricated f-TE devices with three GF values (1.0, 0.56, and 0.25) by solely varying A_p and measured the electric and thermal output at different ΔT values to verify the GF-dependent output characteristics (Fig. 2, C to F, and fig. S5). The trends of P_O, PCE, V_{OC}, and R_{te} for various GF values agreed with the modeling results (Fig. 2, C and D). Generally, PCE is determined by the P_O and input thermal power (i.e., Q_C+ P_O, where Q_C is the output thermal power) (Eq. 4; see Materials and Methods for details). The measured Q_C goes up with increased GF values (GF ≤ 1.0; fig. S5J), indicating similarity to the GF-dependent P_O variations (Fig. 2C). The ratio of P_O/Q_C tends to peak at GF = 0.56 (fig. S5K), which is consistent with the GF-dependent PCE (Fig. 2C), owing to the quasi-linear characteristics between P_O/Q_C and PCE, as experimentally and theoretically verified in fig. S5L. These findings reveal that our device topology co-design approach plays a vital role in synergistic manipulations of P_O and Q_C toward maximized PCE. Here, the deviations between the simulation and measured data (Fig. 2, C and D) were mainly ascribed to the absence of electrical and thermal contact resistances (*18*, *38*). We also measured the electrical contact resistance (R_C) between TE legs and the electrode by using transmission line method (fig. S6; see Materials and Methods for details). In contrast to conventional device (GF = 1.0), where the contact resistance (resistivity) is 1.91 milliohms (113.3 microhm·cm^2) and 1.65 milliohms (77.7 microhm·cm^2) for p-type (A_p = 2.0 mm × 2.0 mm) and n-type leg (A_n = 2.0 mm × 2.0 mm) to the electrode, separately. The proposed device (GF = 0.56) with a lower contact resistance (resistivity) of 1.13 milliohms (43.2 microhm·cm^2) by using co-designed p-type

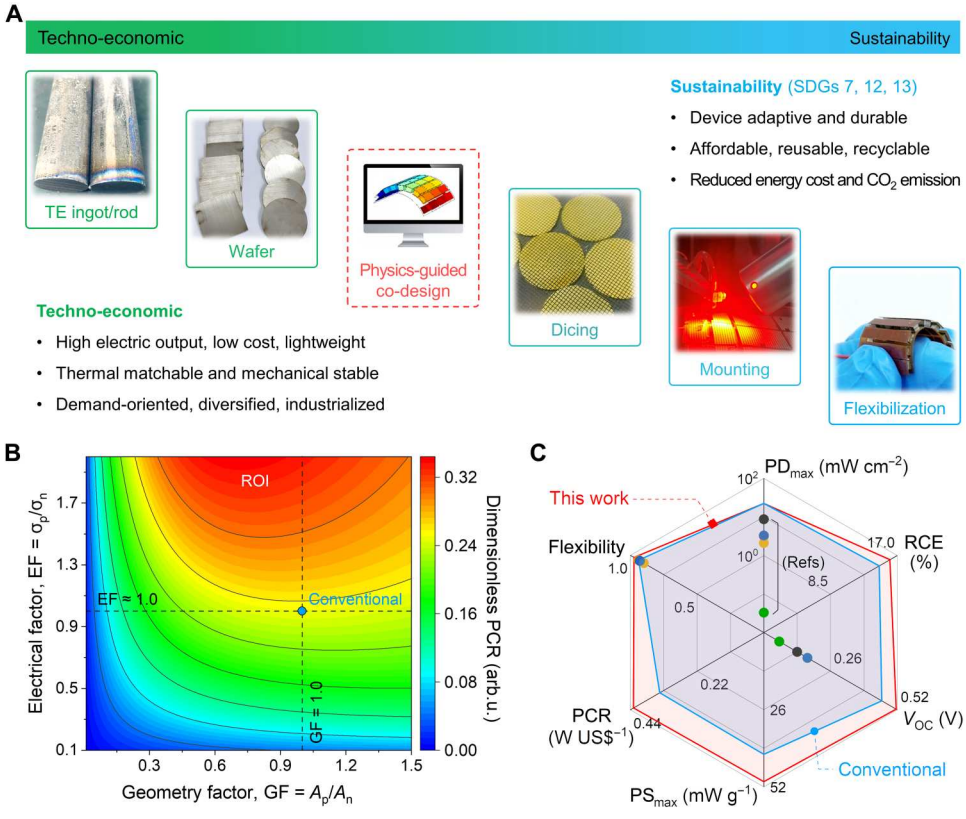

Fig. 1. Physics-guided f-TEs and comparison with conventional designs. (**A**) Illustration of techno-economic sustainability for physics-guided industry-orientated fabrication of f-TEs. Here, the industrial synthesis process from raw materials to TE ingots/rods is not included. SDGs refer to the sustainable development goals (SDG7, Affordable and Clean Energy; SDG12, Responsible Consumption and Production; SDG13, Climate Change) adopted by the United Nations. (**B**) Dimensionless power-cost ratio (PCR) versus geometry and electrical factors. (**C**) Radar plot of key parameters for state-of-the-art comparison of this work (GF < 1.0) and conventional designs (GF = 1.0), where PD_{max}, PS_{max}, and V_{OC} denote the maximum power density, maximum specific power, and open-circuit voltage, respectively. Photo credit: (A) Xixi Liu, Shenzhen Thermo-Electric New Energy Co. Ltd.

leg (A_p = 1.5 mm × 1.5 mm) enables to minimize R_{te} (i.e., ratio of R_C/R_{te}) toward a large P_O and PCE (Eqs. 3 and 16 and Fig. 2, C and D). The slight drop of experimental V_{OC} (Fig. 2D) is attributed to the measurement variation, which agrees with the simulation. In addition, a high R_{te} (low GF value) deteriorates P_O and Q_C (Fig. 2, C and D, and fig. S5), so the GF of ~0.56 is a delicate balance to comprehensively optimize V_{OC}, P_{max}, and PCE_{max} (fig. S7). Notably, PD_{max} for co-designed f-TE device (GF = 0.56) is around 22.31 mW cm^{-2} under ΔT of 73°C, which is around 10-fold greater than that of other bulk material–based devices (Table 1; <100°C low-grade heat harvesting at T_C = 27°C). We then analyzed the electrical output of an f-TE device at GF = 0.56 (Fig. 2, E and F, and figs. S7 and S8). PD_{max} and PCE_{max} increased with a rising ΔT across the device (consistent with Eqs. 2 and 6; see Materials and Methods for details), while the corresponding currents for the two electrical outputs were dissimilar (i.e., $I_{PCE\_max} < I_{P\_max}$) at a specific ΔT. This means that the internal resistance for determining PD_{max} and PCE_{max} was not identical for an invariable load resistance, as revealed by the extracted impedance ratio (fig. S8). From the viewpoint of electrostatics, the GF-dependent output is equivalent to the impedance ratio, and the experimentally obtained λ_{P_max}= 1 and $\lambda_{PCE\_max} > 1$ was consistent with the modeling and industrial measurements (*49*). Furthermore, our co-designed f-TE device (GF = 0.56) is enabled to generate an estimated power of 0.475 mW at a 5°C attainable temperature difference between body skin and ambient (fig. S7C). This value is sufficient to power a kind of low-power wearable electronics (*26*, *43*, *50*), such as temperature or relative humidity sensors and smartwatches.

In addition, our developed strategy can be generalized to other TE materials/devices apart from bismuth telluride. The GF-dependent modeling of PD_{max} and PCE_{max} using representative inorganic materials [e.g., PbTe (*12*), Mg_3Sb_2 (*6*, *7*), and SnSe (*8*)] and organic materials {poly[A_x(M-ett)] (*15*)} is shown in fig. S9. The GF values for PD_{max} and PCE_{max} are less than 1.0 and vary with different materials. Specifically, the ROI for PbTe, Mg_3Sb_2, SnSe, and poly[Cu_x-(Cu-ett)]/poly[Na_x(Ni-ett)] is dissimilar, i.e., GF = 0.25, 0.4, 0.55, and 0.65, respectively. These results suggest that the fundamentals of GF-dependent TEs (Fig. 1B, fig. S2B, and Eq. 12; see Materials and Methods for details) are applicable to all p-n paired materials/devices. The conclusion remains consistent to that of Bi_2Te_3 materials, i.e., a rationalized thin p-type leg benefits to reduce material usage while boosting the electricity generation toward sustainable heat harvesting. Besides, in terms of low-grade heat recovery, Bi_2Te_3 is a priority candidate owing to its high TE performance and cost-effectiveness compared with other materials (figs. S4 and S9). On the other side, the TE device fabrication procedure normally follows the "material-to-device" route with known material

Table 1. State-of-the-art comparison of output performance and cost-effectiveness for conventional and proposed f-TE devices (T_H= 100°C, T_C= 27°C).

GF	PD_{max} (mW cm^{-2})	PS_{max} (mW g^{-1})	PCR (W US^{-1})	RCE (%)	V_{OC} (V)	Flexibility ($\Delta R/R_0$)	Reference	Notes*
1.0	0.03	–	–	–	0.06	–	(*64*)	Estimated
1.0	2.10	–	–	–	0.17	0.90	(*65*)	Estimated
1.0	3.18	–	–	–	–	0.94	(*26*)	Estimated
1.0	3.30	–	–	–	0.17	0.93	(*66*)	Estimated
1.0	8.65	–	–	–	0.13	0.93	(*42*)	Estimated
1.0	22.31	41.06	0.34	14.71	0.46	0.94	This work	Measured
0.56	22.31	50.27	0.43	16.06	0.52	0.97	This work	Measured

*"Estimated" means that PD_{max} of the f-TE device was estimated from a quadratic relationship at a temperature gradient of 73°C (Eq. 3; see Materials and Methods for details), whereas V_{OC} was estimated from a linear fitting at open-circuit state (where the current is zero; Eq. 1).

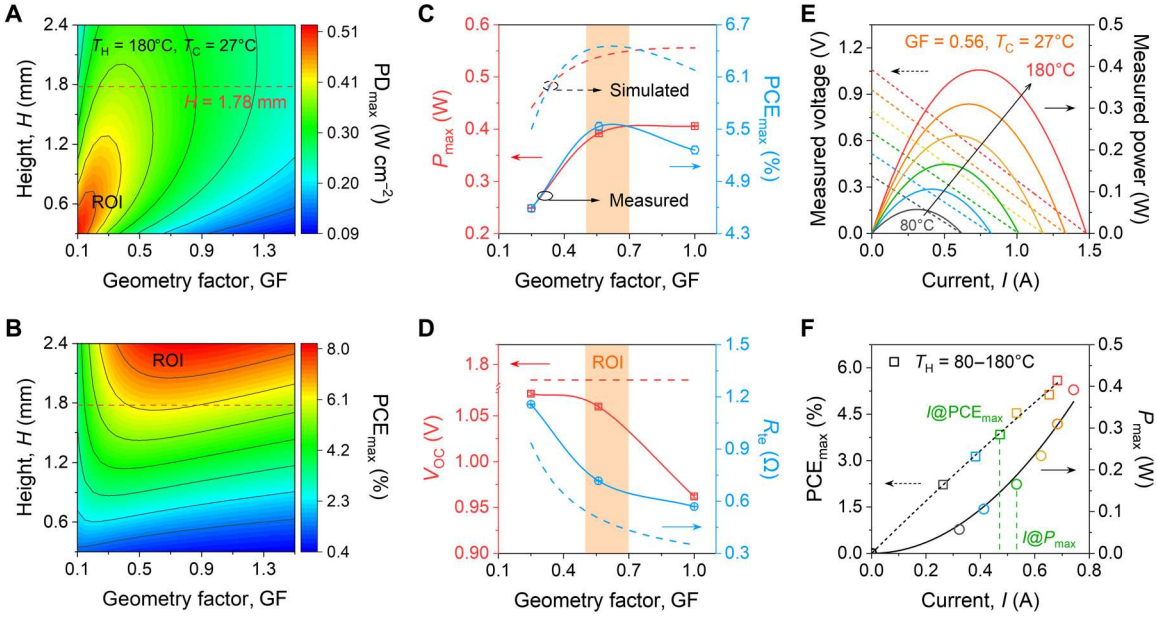

Fig. 2. Physical modeling and experimental verification. GF-dependent (**A**) PD_{max} and (**B**) maximum PCE from simulations. The height (H = 1.78 mm) was recommended from typical commercial TE modules. PD_{max} and PCE (**C**), as well as (**D**) V_{OC} and internal resistance at different GF values. Dashed lines, simulated result; solid lines, measured data. ROI refers to the region of interest used for optimum device design. (**E**) Measured voltage and power versus output current at different temperature gradients. (**F**) Maximum PCE and maximized power variations with output current for various temperature differences, where $I_{PCE\_max} < I_{P\_max}$.

properties, so the EF is unchangeable for specific materials, although it affects the PCR (Fig. 1B). This signifies that our proposed strategy could offer an unconventional way, i.e., "device-to-material" to optimize the EF value, thus guiding material synthesis and property manipulation under given GF and PCR values.

Flexibility, stability, and durability characterizations

Aside from the leveraged output power via physics-guided device topology rationalization, the flexibility, stability, and durability also play crucial roles in practical applications. First, the flexibility of the proposed f-TE device with an optimum geometry (GF = 0.56) was quantified at various bending radii and cycles (Fig. 3A; see Materials and Methods for details). The modest variation of the internal resistance during bending tests indicated that the end-to-end electrical interconnection between the inorganic TE legs and flexible electrodes is adequately stable and suitable for the thermal energy harvesting of curved heat sources. Because of the reduced size of p-type legs, the fill factor decreased as well (fig. S2B). The enlarged air gap between adjacent TE legs could benefit the device bending under an external stimulus. Consequently, we investigated the resistance change (R/R_0) of an f-TE device with (GF = 0.56) and without (conventional, GF = 1.0) physics-guided co-design after 1000-cycle bending tests (r = 5 mm). R/R_0 of the optimized f-TE device (2.62%) was less than that of the conventional device, which was identified by the strain modeling as well (Fig. 3B). Specifically, under a constant external pressure (fig. S10; see Materials and Methods for details), the volumetric strain of a conventional device is greater than that of the developed f-TE device.

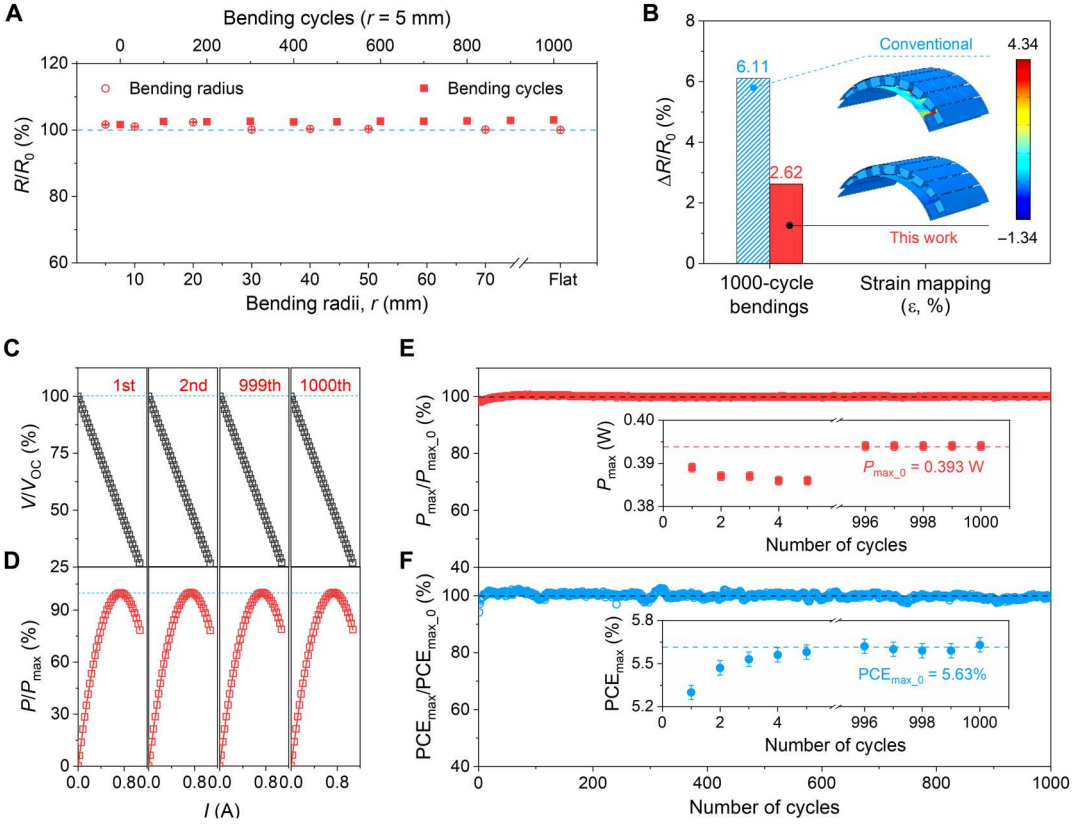

Fig. 3. Flexibility, stability, and durability characterizations of f-TE devices at GF = 0.56. (**A**) Resistance variations for various bending radii and cycles (r = 5 mm). (**B**) Relative resistance changes after 1000-cycle bending (left) and strain mapping (ε, right) for the conventional (GF = 1.0) and proposed (GF = 0.56) devices. Ratio of output voltage and V_{OC} (**C**), as well as (**D**) power/P_{max} versus current for the first and last two measurements of 1000-cycle stability evaluation. Maximum power (**E**) and (**F**) maximum PCE variations for 1000-cycle durability test. Inset, the first and last five measured data.

These results elucidate that our approach with a rationalized geometry co-design not only offered a high electrical output but also contributed to strain propagation across the device for superior flexibility. This unprecedented finding could pave a feasible route for co-designing high-performance f-TEs in the absence of material tailoring (i.e., complex manipulation of carrier concentration and electronic structure). Moreover, to verify the device stability and durability for <100°C waste heat harvesting, the acceleration testing of an f-TE device (GF = 0.56) was evaluated over 1000 thermal cycles at a large ΔT of 153°C (fig. S11A). The voltage-current and power-current plots of the first and last two measurements showed a cycle-independent steady output (Fig. 3, C and D) and negligible P_{max}, PCE_{max}, V_{OC}, and R_{te} variations (Fig. 3, E and F, and fig. S11). The slight fluctuation of P_{max}, PCE_{max}, V_{OC}, and R_{te} for the first five tests (insets of Fig. 3, E and F, and fig. S11) is mainly ascribed to the heat flow variation across the device at initial states, which tends to be stable under continuous measurements.

Techno-economic sustainability estimation

Furthermore, in practice, to promote the attained high-performance f-TEs in industrial implementation for waste heat harvesting, the cost-effectiveness and sustainable production are prior considerations toward affordable energy supply and carbon emission reduction. Therefore, we focus on how the physics-guided co-design contributes to the techno-economic sustainable industrialization of f-TE devices. Specifically, a typical large-scale industrial production flow of TE materials was introduced, and the synthesis procedures, as well as corresponding electricity consumption, were analyzed (Fig. 4A; see Materials and Methods for details). In terms of commercial bismuth telluride alloys, the p-type material (orange block) is usually prepared via the hot-press method, and the n-type material (green block) is synthesized by the zone-melting technique. These different synthesis approaches and processes lead to distinct TE properties (fig. S4) and electricity consumption demand (table S2). Compared to conventional designs, the reduced material usage of the p-type legs (by 44%) in our f-TE device offers higher RCEs (Fig. 4B) over a wide temperature range (ΔT up to 153°C for T_C = 27°C). This suggested that the developed device (GF = 0.56) is capable of highly efficient heat-to-electricity conversion at a given temperature gradient and consistent material properties (*16*). The minimal energy consumption (W_{min}) for large-scale p-type ingot/rod production from raw materials would be reduced by 19.3% if our solution were deployed (see Materials and Methods for details). In addition, we estimated the cost savings, electricity savings, and equivalent CO_2 emission reduction per output power of the developed f-TE device with ΔT of 73°C for low-grade heat harvesting (T_H < 100°C). The results showed that 0.61 US\$ W^{-1} of cost savings, 0.24 kWh W^{-1} of electricity savings, and 0.17 kg W^{-1} carbon emission reduction could be achieved for an f-TE device by solely introducing a physics-guided co-design

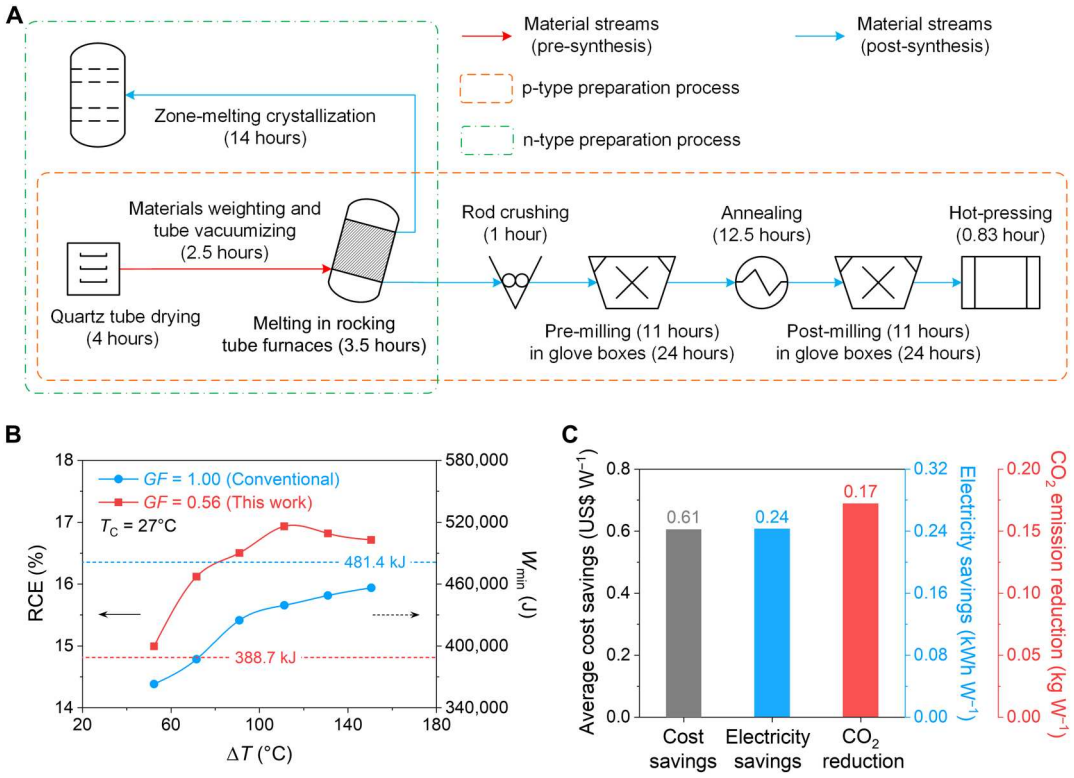

Fig. 4. Techno-economics estimation for industry-orientated sustainable heat harvesting. (**A**) Typical large-scale industrial production flows of p- and n-type TE ingots from raw materials. (**B**) RCE (left) and estimated minimal energy consumption (right) of conventional and proposed devices at different temperature gradients. The RCE can be calculated from the ratio between PCE_{max} and the Carnot efficiency (Eq. 7). (**C**) Estimated average cost savings, electricity savings, and CO_2 emission reduction per watt by deploying the proposed f-TE device (GF = 0.56). Details can be found in Table 2 and table S2.

(Fig. 4C and Table 2). Our delivered strategy, which realized cost-effective, high-output, f-TEs, is facile, universal, and fundamentally different from traditional approaches. In recent years, although the material cost of TE devices has been reduced by using abundant elements (e.g., Mg_3Sb_2, SnS, SnSe, half-Heusler compounds, silicide, and polymers) (*5*, *9*, *14*, *51*–*55*), the industrialization remains challenging. Since no headway has been made so far in their corresponding large-scale production process, and their demands/markets are unclear (*33*, *56*), academia and industry are urged to diversify their research focus past the one-and-only commercialized room temperature Bi_2Te_3 materials.

DISCUSSION

In summary, we investigated a nonunity, co-designed geometry of unconventional f-TEs to address the long-standing challenges in cost-effective, sustainable, and low-grade heat harvesting. The physics-guided device rationalization reduces the usage of TE materials by 44% (p-type) while barely deteriorating the electrical output, in contrast to conventional approaches. This "decoupled" power output and cost account for an unprecedented PCR enhancement of 25.3%, minimal energy consumption reduction of 19.3%, electricity savings of 0.24 kWh W^{-1}, and carbon emission reduction of 0.17 kg W^{-1} for large-scale industrial production. Further

Table 2. Estimation of cost savings, electricity savings, and CO_2 emission reduction of conventional and proposed f-TE devices.

f-TE devices	Mass, p-type legs (g)	Mass, n-type legs (g)	PCR (W US^{-1})	Cost per watt (US$ W^{-1})	Electricity usage per watt (kWh W^{-1})	CO_2 emission per watt (kg W^{-1})
GF = 1.0	1.048	1.259	0.332	3.009	1.262	0.894
GF = 0.56	0.583	1.259	0.416	2.403	1.019	0.722
Savings*	0.465 (−44.3%)	0	0.084 (+25.3%)	0.606 (−20.1%)	0.24 (−19.3%)	0.17(−19.3%)

*The symbol in savings indicates the corresponding proportion of increase ("+") or decrease ("−"). The output power at T_H = 100°C and T_C = 27°C was used for estimation. The commercial electricity and raw materials (bismuth telluride) prices are 0.23 $ kWh^{-1} and 125 $ kg^{-1} (*33*), respectively. The cost of substrates, electrodes, and solder was not included in the estimation. In contrast to the conventional design (GF = 1.0), the proposed device (GF =0.56) contributed to p-type materials usage reduction, while the dimension of n-type legs remained consistent, so the overall electricity consumption reduction (i.e., equivalent carbon emission minimization and energy savings) and cost savings were dominated by p-type materials.

development of flexible electrical interconnected electrodes and polymer substrates, as well as demand-oriented device diversification, is a promising approach to advance the industrial sustainable low-grade heat-to-electricity conversion. This upcycling of low-grade waste heat through physics-guided rationalization of the device topology also creates a previously unidentified paradigm for other energy harvesting and management frontiers, e.g., device-guided material synthesis, TE cooling, transverse TEs, thermocells, semiconductors, and electronics heat management.

MATERIALS AND METHODS

Fundamentals of GF-dependent PCR analysis

On the basis of the Seebeck effect for spatial heat harvesting, the electric potential of a TE uni-couple is governed by $S_{pn}\Delta T$, where S_{pn} is the sum of the Seebeck coefficients of p- and n-type TE legs, and ΔT denotes the spatial temperature gradient across the hot (T_H) and cold (T_C) sides of TE legs. The output voltage (V_o) of a uni-couple is given by

$$V_o = S_{pn}\Delta T - IR_{te} \tag{1}$$

where V_o is proportional to the current flowing across the TE uni-couple under a known internal resistance R_{te}. In addition, the P_o can be derived from the voltage-current relationship and is expressed as

$$P_o = I^2R_L = S_{pn}\Delta T \cdot I - I^2R_{te} \tag{2}$$

Then, the maximum output power (P_{max}) is determined from Eq. 2, as long as the external load impedance (R_L) equals R_{te} (i.e., the impedance ratio $\lambda = R_L/R_{te}$ and $\lambda_{P_{max}} = 1$)

$$P_{max} = \frac{S_{pn}^2\Delta T^2}{4R_{te}} \tag{3}$$

Furthermore, PCE of a TE device can be estimated by

$$\mathrm{PCE}\ (\%) = \frac{P_o}{Q_H} = \frac{P_o}{Q_C + P_o} \tag{4}$$

Q_H and Q_C are the hot-side and cold-side thermal powers, respectively, and can be derived from the Seebeck effect, Peltier effect, and Joule heating, as follows

$$\begin{cases} Q_H = S_{pn}T_HI - \frac{1}{2}I^2R_{te} + K(T_H - T_C) \\ Q_C = S_{pn}T_CI + \frac{1}{2}I^2R_{te} + K(T_H - T_C) \end{cases} \quad \text{(5a) and (5b)}$$

Consequently, by substituting Eqs. 2, 5a, and 5b into Eq. 4, PCE can be rewritten as

$$\mathrm{PCE} = \frac{T_H - T_C}{T_H}\left\{\frac{R_L}{R_{te}}\left[\left(1 + \frac{R_L}{R_{te}}\right) - \frac{T_H - T_C}{2T_H} + \frac{(1 + R_L/R_{te})^2}{ZT_H}\right]^{-1}\right\} \tag{6}$$

This formula can be simplified by applying $\lambda = R_L/R_{te}$, and the maximized PCE is obtained in the condition of $\partial(\mathrm{PCE})/\partial\lambda = 0$

$$\begin{aligned} \mathrm{PCE}_{max} &= \frac{T_h - T_c}{T_h}\frac{\lambda_{PCE\_max} - 1}{\lambda_{PCE\_max} + T_c/T_h} \\ &= \eta_{Carnot}\frac{\lambda_{PCE\_max} - 1}{\lambda_{PCE\_max} + T_c/T_h} \end{aligned} \tag{7}$$

where η_{Carnot} is the Carnot efficiency, and the irreversibility of TE generators (heat engines) is reported as the RCE that is given by the ratio between PCE and η_{Carnot} (*16*, *32*, *57*), i.e., $\mathrm{RCE} = \mathrm{PCE}/\eta_{Carnot}$. $\lambda_{PCE\_max} = \sqrt{1 + ZT_{ave}} > 1 = \lambda_{P\_max}$, where $ZT_{ave} = \frac{1}{T_h - T_c}\int_{T_c}^{T_h} ZT\mathrm{d}T$. From the viewpoint of the pure resistive circuit and Kirchhoff's laws, these mathematical derivations suggest that the internal resistances for the maximum output power (P_{max}) and PCE_{max} are different, i.e., $R_{PCE\_max} > R_{P\_max}$ for a given R_L. In terms of the GF-dependent characteristics of the resistance (fig. S2), the distinct internal resistances of P_{max} and PCE_{max} eventually reveal that the device geometry demands for the two goals are entirely dissimilar. For instance, the cross-sectional area ratio between the p-type (A_p) and n-type (A_n) legs, i.e., (GF = A_p/A_p), substantially varies the total resistance and output of the TE device for known materials (invariable, $\mathrm{EF} = \sigma_p/\sigma_n$)

$$\begin{aligned} R_{te} &= \frac{H}{\sigma_pA_p} + \frac{H}{\sigma_nA_n} = \frac{H}{A_n}\left(\frac{1}{\sigma_p\mathrm{GF}} + \frac{1}{\sigma_n}\right) \\ &= \frac{H}{A_n\sigma_n}\left(\frac{1}{\mathrm{EF}\cdot\mathrm{GF}} + 1\right) \end{aligned} \tag{8}$$

Furthermore, to quantify how the GF variation affects the PCR, the GF-dependent PCR of a TE device is estimated. First, the cost [C ($)] of a typical TE device is given in consideration of the volumetric cost (C''') and area cost (C'') (*46*). The volumetric cost consists of the cost of TE materials, manufacturing costs (e.g., hot pressing and zone melting), and other costs that scale with the amount of TE materials. By contrast, the areal cost includes areal manufacturing costs (e.g., dicing, cutting, and mounting), metallization, flexibilization, and other scales with the device area. The overall cost can be shown as follows

$$C[\$] = (C'''H + C'')(A_p + A_n) = (C'''H + C'')(1 + \mathrm{GF})A_n \tag{9}$$

where H refers to the height of the TE legs. The PCR (W $\$^{-1}$) is given by the combination of Eqs. 3 and 9

$$\mathrm{PCR}[\mathrm{W}\ \$^{-1}] = \frac{P_{max}}{C} = \frac{S_{pn}^2\Delta T^2}{(C'''H + C'')(1 + \mathrm{GF})A_n(4R_{te})} \tag{10}$$

By substituting Eq. 8 into Eq. 10, the PCR can be rewritten as

$$\mathrm{PCR}[\mathrm{W}\ \$^{-1}] = \frac{S_{pn}^2\Delta T^2\sigma_n}{4H(C'''H + C'')}\left[(1 + \mathrm{GF})\left(1 + \frac{1}{\mathrm{EF}\cdot\mathrm{GF}}\right)\right]^{-1} \tag{11}$$

For a unit cost, $PCR_0 = (S_{pn}^2\Delta T^2\sigma_n)/[4H(C'''H + C'')]$, the dimensionless PCR is given by

$$\frac{\mathrm{PCR}}{\mathrm{PCR}_0} = \left[(1 + \mathrm{GF})\left(1 + \frac{1}{\mathrm{EF}\cdot\mathrm{GF}}\right)\right]^{-1} \tag{12}$$

Thus, the dimensionless PCR is GF dependent for specific TE materials (EF is unchangeable), and the geometry co-design is crucial and universal for desirable cost-effectiveness and power output.

Physics-guided finite element modeling

The finite element modeling of geometry-dependent TE output was performed by using COMSOL Multiphysics software with Heat Transfer in Solids, Electric Currents, and Electrical Circuit (*58*).

Specifically, the Heat Transfer in Solids was used to model the heat transfer in solid domains concerning the heat conduction, convection, and radiation. The governing equation of heat transfer with external heat source (Q_e) can be given from the differential form of Fourier′s law

$$\begin{cases} \rho C_p u \cdot \nabla T + \nabla \cdot q = Q_e \\ q = -\kappa \nabla T \end{cases} \quad (13)$$

in which ρ, C_p, and u are density, specific heat, and thermal diffusivity, respectively; κ is the thermal conductivity; and T is the absolute temperature. The second module of Electric Currents was used to solve the current conservation equation in accordance with Ohm′s law, and the governing equation is given as

$$\begin{cases} \nabla J = Q_j \\ J = \sigma E + J_e \\ E = -\nabla V \end{cases} \quad (14)$$

where J, J_e, and Q_j are induced electric current, external current source, and current source, respectively, and σ, E, and V are electrical conductivity, electric field, and electric potential, respectively. The last module of Electrical Circuit was used to model a load resistor for recording the voltage and current output under electrical matching conditions. Considering the thermodynamic relation of Seebeck effect, Peltier effect, and Thomson effect, the governing equations for TE modeling can be written as

$$\begin{cases} q = PJ \\ P = ST \\ J_e = -\sigma S \nabla T \end{cases} \quad (15)$$

where P, S, and T are Peltier coefficient, Seebeck coefficient, and absolute temperature, respectively. Thus, the target for device topology co-design of TEs was simplified to solve the geometry-dependent current density and heat flux across the device with variable dimensions of TE legs by using finite element modeling under stationary heat transfer, as illustrated in the flowchart (fig. S3). For materials selection, the measured TE properties of bismuth telluride (fig. S4) and other parameters from the COMSOL material library were used in the simulation. Moreover, to determine how the optimized geometry affected the bendability of the f-TE device, the strain mapping of conventional and optimized devices under an external bending/contact pressure (2 kPa) (*59*) was analyzed using the Heat Transfer and Solid Mechanics modules. The hot- and cold-side temperatures of f-TE device remained constant ($T_H = T_C = 27$°C, consistent with the room temperature) to minimize the thermal expansion. There were two stress boundaries introduced (fig. S10), i.e., pressure load layers and constraint layers, for strain modeling.

f-TE device fabrication and characterization

Commercial $Bi_{0.4}Sb_{1.6}Te_3$ and $Bi_2Te_{2.85}Se_{0.15}$ materials (provided by Shenzhen Thermo-Electric New Energy Co. Ltd.) were used for p- and n-type TE leg fabrications, respectively. For materials characterization, the Seebeck coefficient and the electrical conductivity were measured simultaneously using a four-probe static direct current method (commercial instrument, ZEM3, ULVAC-RIKO) with a sample size of 2 mm × 2 mm × 10 mm, in which the corresponding uncertainty was 3 and 5%, respectively. The thermal conductivity was indirectly determined using the following equation: $\kappa = D \cdot \rho \cdot C_p$, where the thermal diffusivity (D) was obtained via the laser flash method (commercial instrument, LFA457, NETZSCH) with a sample size of 6 mm × 6 mm × 1.5 mm and an uncertainty of 5%. The density (ρ) was measured by the Archimedes method, and the specific heat (C_p) was obtained from previous work (*60*). The uncertainty of measured temperatures is 1%. The sample orientation used for thermal and electrical measurements was illustrated in the insets of fig. S4. The device ZT and efficiency were estimated by using the ZT calculator (*61*). Therefore, according to the law of propagation of uncertainty (*62*), the combined uncertainty of PF and ZT were estimated at 11 and 16%, respectively. For device fabrication, the dimensions of the n-type TE leg (2.0 mm × 2.0 mm × 1.78 mm) were fixed, and we solely varied the dimensions of the p-type legs from 2.0 mm × 2.0 mm × 1.78 mm (GF = 1.0) to 1.5 mm × 1.5 mm × 1.78 mm (GF = 0.56) and 1.0 mm × 1.0 mm × 1.78 mm (GF = 0.25). The fabrication procedure of the f-TE devices can be found in our previous work (*37*). The electrical outputs of the TE modules (25 mm × 19 mm × 1.9 mm) were evaluated by using a commercial instrument (PEM2, ULVAC-RIKO) in a vacuum atmosphere with an uncertainty of 10%. The output heat flux of the TE device was acquired using a typical technique, i.e., the steady-state plate method and one-dimensional heat conduction. Specifically, the TE device was sandwiched in a heater and a cooler (copper block with controlled water cooling). There are three thermocouples vertically positioned inside the copper block with an interval of 5 mm, and the temperature was obtained under a steady state. The output heat flux (q_C) can be given on the basis of Fourier′s law of heat conduction, i.e., $q_C = \kappa_{Cu} \Delta T/d$, where κ_{Cu} is the thermal conductivity of copper block and d is the spatial difference between adjacent thermocouples. The temperature, output voltage, and internal resistance were concurrently recorded by varying the current with a step of 0.03 A. Then, PCE was calculated on the basis of Eq. 4. In terms of low-grade heat harvesting and one-dimensional steady-state heat transfer, the heat loss (thermal radiation and convection) is negligible and not considered in the measurement. Moreover, we examined the contact behavior of fabricated f-TE devices by using transmission line method. As illustrated in fig. S6, considering neighboring TE legs located on an electrode, the measured total resistance (R_{total}) across neighboring TE legs can be given as in (*63*),

$$R_{total} = 2R_{leg} + 2R_C + R_{ele} \quad (16)$$

in which R_{leg} is the resistance of TE leg due to contact, R_C is the contact resistance associated with the metal/semiconductor interface, and R_{ele} is the usual electrode resistance. Normally, R_{leg} is known according to the σ of TE materials (fig. S4B), and $R_{ele} = R_E L/W$ for a given electrode with limited lengths (L) and widths (W). Thereby, Eq. 16 can be simplified as

$$R_T = L\frac{R_E}{W} + 2R_C \quad (17)$$

where $R_T = R_{total} - 2R_{leg}$ and is proportional to L, R_C and transfer length (L_T) can be extracted separately from the intercept at vertical and horizontal axes of the linear curve, and the slope is the sheet resistance of the electrode. Then, the contact resistivity (ρ_C) can be calculated, i.e., $\rho_C = R_C L_T W$ (*63*). In our experiments, five TE legs (p-type, A_p = 1.5 mm × 1.5 mm, corresponding GF = 0.56) were soldered on a Cu strip with spacings of 2.5, 5.0, 10.0, and 20.0 mm to form metal-semiconductor contacts. R_T of p-type legs

to the electrode across different spacings was measured by using an inductance-capacitance-resistance (LCR) meter (U2830, EUCOL) and plotted in fig. S6B. The measurement of R_C and L_T for other p-type leg (A_p = 2.0 mm × 2.0 mm, corresponding GF =1.0) and n-type leg (A_n = 2.0 mm × 2.0 mm) to the electrode was performed by a consistent manner.

Flexibility, stability, and durability verifications

The flexibility characterization of the f-TE devices was conducted in a homemade system, where a fatigue analyzer (PA2021-0004, Prime-Ace Tech) with adjustable bending radii and speeds, as well as an LCR meter (U2830, EUCOL), was used for resistance measurements. The flexibility used for state-of-the-art comparison was calculated from R/R_0 of f-TE devices after 1000 bending cycles with a bending radius of 5 mm (*20*). Moreover, the stability and durability of devices were characterized by using a PEM2 data logger (ULVAC-RIKO) in a vacuum atmosphere. The T_H and T_C values of the device were maintained at 180° and 27°C, respectively, for the acceleration test of the low-grade waste heat harvesting. The electrical measurements were performed for over 1000 cycles using the LabView software.

Estimation of cost savings, electricity savings, and CO_2 emission reduction

The reduced material usage of the p-type TE legs from the physics-guided optimal GF (i.e., GF = 0.56) contributed to practical cost savings, electricity savings, and CO_2 emission reduction. On the basis of the typical industrial production flow (Shenzhen Thermo-Electric New Energy Co. Ltd.), the cost savings (raw TE materials and device components), electricity savings (electricity consumption of TE ingot fabrication), and equivalent CO_2 emission (1 kWh electricity = 0.709 kg CO_2; https://epa.gov/energy/greenhouse-gas-equivalencies-calculator) per power output of an optimized f-TE device were estimated. Details can be found in table S2. The minimal energy consumption (W_{min}) of large-scale industrial production for conventional and developed f-TE devices is estimated as

$$W_{min} = \frac{m_p}{M_p}\sum_{i=1}^{i=10} P_p^i t_p^i + \frac{m_n}{M_n}\sum_{j=1}^{j=4} P_n^j t_n^j \quad (18)$$

where the first and second terms refer to the electricity usage of p- and n-type TE legs per device, respectively. In this work, the dimensions of p-type legs were varied, whereas those of the n-type legs remained constant. m_p is the mass of the p-type TE legs; M_p is the total mass of the p-type ingots/rods using large-scale industrial production (orange block; Fig. 4A); P_p^i and t_p^i are the electric power and the corresponding operational duration of the specific equipment, respectively; and i is the index number of the equipment. Similarly, m_n is the mass of the n-type TE legs; M_n is the total mass of the n-type ingots/rods in large-scale industrial production (green block; Fig. 4A); P_n^j and t_n^j are the electric power and the corresponding operational duration of the specific equipment, respectively; and j is the index number of the equipment. Consequently, W_{min} is mainly dependent on m_p of the f-TE devices.

Supplementary Materials

This PDF file includes:

Figs. S1 to S11
Tables S1 and S2

REFERENCES AND NOTES

1. I. Johnson, W. T. Choate, A. Davidson, *Waste Heat Recovery. Technology and Opportunities in U.S. Industry* (BCS Inc., 2008); https://osti.gov/servlets/purl/1218716.
2. International Energy Agency, *Energy Efficiency 2021* (International Energy Agency, 2021).
3. International Energy Agency, *Renewables 2021* (International Energy Agency, 2021).
4. J. Duan, B. Yu, L. Huang, B. Hu, M. Xu, G. Feng, J. Zhou, Liquid-state thermocells: Opportunities and challenges for low-grade heat harvesting. *Joule* **5**, 768–779 (2021).
5. C. Zhou, Y. K. Lee, Y. Yu, S. Byun, Z.-Z. Luo, H. Lee, B. Ge, Y.-L. Lee, X. Chen, J. Y. Lee, O. Cojocaru-Mirédin, H. Chang, J. Im, S.-P. Cho, M. Wuttig, V. P. Dravid, M. G. Kanatzidis, I. Chung, Polycrystalline SnSe with a thermoelectric figure of merit greater than the single crystal. *Nat. Mater.* **20**, 1378–1384 (2021).
6. Z. Liu, N. Sato, W. Gao, K. Yubuta, N. Kawamoto, M. Mitome, K. Kurashima, Y. Owada, K. Nagase, C.-H. Lee, J. Yi, K. Tsuchiya, T. Mori, Demonstration of ultrahigh thermoelectric efficiency of ~7.3% in Mg_3Sb_2/MgAgSb module for low-temperature energy harvesting. *Joule* **5**, 1196–1208 (2021).
7. Z. Ren, J. Shuai, J. Mao, Q. Zhu, S. Song, Y. Ni, S. Chen, Significantly enhanced thermoelectric properties of p-type Mg_3Sb_2 via co-doping of Na and Zn. *Acta Mater.* **143**, 265–271 (2018).
8. C. Chang, M. Wu, D. He, Y. Pei, C.-F. Wu, X. Wu, H. Yu, F. Zhu, K. Wang, Y. Chen, L. Huang, J.-F. Li, J. He, L.-D. Zhao, 3D charge and 2D phonon transports leading to high out-of-plane *ZT* in n-type SnSe crystals. *Science* **360**, 778–783 (2018).
9. T. Zhu, C. Fu, H. Xie, Y. Liu, X. Zhao, High efficiency half-heusler thermoelectric materials for energy harvesting. *Adv. Energ. Mater.* **5**, 1500588 (2015).
10. H. Zhu, J. Mao, Z. Feng, J. Sun, Q. Zhu, Z. Liu, D. J. Singh, Y. Wang, Z. Ren, Understanding the asymmetrical thermoelectric performance for discovering promising thermoelectric materials. *Sci. Adv.* **5**, eaav5813 (2019).
11. C. J. Vineis, A. Shakouri, A. Majumdar, M. G. Kanatzidis, Nanostructured thermoelectrics: Big efficiency gains from small features. *Adv. Mater.* **22**, 3970–3980 (2010).
12. P. Jood, M. Ohta, A. Yamamoto, M. G. Kanatzidis, Excessively doped PbTe with Ge-induced nanostructures enables high-efficiency thermoelectric modules. *Joule* **2**, 1339–1355 (2018).
13. F. Kim, B. Kwon, Y. Eom, J. E. Lee, S. Park, S. Jo, S. H. Park, B.-S. Kim, H. J. Im, M. H. Lee, T. S. Min, K. T. Kim, H. G. Chae, W. P. King, J. S. Son, 3D printing of shape-conformable thermoelectric materials using all-inorganic Bi_2Te_3-based inks. *Nat. Energy* **3**, 301–309 (2018).
14. Z. Bu, X. Zhang, Y. Hu, Z. Chen, S. Lin, W. Li, C. Xiao, Y. Pei, A record thermoelectric efficiency in tellurium-free modules for low-grade waste heat recovery. *Nat. Commun.* **13**, 237 (2022).
15. Y. Sun, P. Sheng, C. Di, F. Jiao, W. Xu, D. Qiu, D. Zhu, Organic thermoelectric materials and devices based on *p*- and *n*-type poly(metal 1,1,2,2-ethenetetrathiolate)s. *Adv. Mater.* **24**, 932–937 (2012).
16. B. Yu, J. Duan, H. Cong, W. Xie, R. Liu, X. Zhuang, H. Wang, B. Qi, M. Xu, Z. L. Wang, J. Zhou, Thermosensitive crystallization-boosted liquid thermocells for low-grade heat harvesting. *Science* **370**, 342–346 (2020).
17. Y. Han, J. Zhang, R. Hu, D. Xu, High-thermopower polarized electrolytes enabled by methylcellulose for low-grade heat harvesting. *Sci. Adv.* **8**, eabl5318 (2022).
18. G. J. Snyder, Energy harvesting technologies, in *Energy Harvesting Technologies*, S. Priya, D. J. Inman, Eds. (Springer, 2009), vol. 3, chap. 11, pp. 325–336.
19. S. Liu, Y. Yang, H. Huang, J. Zheng, G. Liu, T. H. To, B. Huang, Giant and bidirectionally tunable thermopower in nonaqueous ionogels enabled by selective ion doping. *Sci. Adv.* **8**, eabj3019 (2022).
20. W. Ren, Y. Sun, D. Zhao, A. Aili, S. Zhang, C. Shi, J. Zhang, H. Geng, J. Zhang, L. Zhang, J. Xiao, R. Yang, High-performance wearable thermoelectric generator with self-healing, recycling, and Lego-like reconfiguring capabilities. *Sci. Adv.* **7**, eabe0586 (2021).
21. T. Ding, K. H. Chan, Y. Zhou, X.-Q. Wang, Y. Cheng, T. Li, G. W. Ho, Scalable thermoelectric fibers for multifunctional textile-electronics. *Nat. Commun.* **11**, 6006 (2020).
22. T. Sun, B. Zhou, Q. Zheng, L. Wang, W. Jiang, G. J. Snyder, Stretchable fabric generates electric power from woven thermoelectric fibers. *Nat. Commun.* **11**, 572 (2020).
23. B. Russ, A. Glaudell, J. J. Urban, M. L. Chabinyc, R. A. Segalman, Organic thermoelectric materials for energy harvesting and temperature control. *Nat. Rev. Mater.* **1**, 16050 (2016).
24. L. Fu, K. Park, S.-I. Kim, B. Kim, H. Y. Song, W. Choi, Y.-M. Kim, J.-Y. Hwang, K. H. Lee, S. W. Kim, High-performance bismuth antimony telluride thermoelectric membrane on curved and flexible supports. *ACS Energy Lett.* **6**, 2378–2385 (2021).

25. Y. Ding, Y. Qiu, K. Cai, Q. Yao, S. Chen, L. Chen, J. He, High performance n-type Ag_2Se film on nylon membrane for flexible thermoelectric power generator. *Nat. Commun.* **10**, 841 (2019).
26. S. Hong, Y. Gu, J. K. Seo, J. Wang, P. Liu, Y. S. Meng, S. Xu, R. Chen, Wearable thermoelectrics for personalized thermoregulation. *Sci. Adv.* **5**, eaaw0536 (2019).
27. Q. Jin, S. Jiang, Y. Zhao, D. Wang, J. Qiu, D.-M. Tang, J. Tan, D.-M. Sun, P.-X. Hou, X.-Q. Chen, K. Tai, N. Gao, C. Liu, H.-M. Cheng, X. Jiang, Flexible layer-structured Bi_2Te_3 thermoelectric on a carbon nanotube scaffold. *Nat. Mater.* **18**, 62–68 (2018).
28. L. Wang, Z. Zhang, L. Geng, T. Yuan, Y. Liu, J. Guo, L. Fang, J. Qiu, S. Wang, Solution-printable fullerene/TiS_2 organic/inorganic hybrids for high-performance flexible n-type thermoelectrics. *Energ. Environ. Sci.* **11**, 1307–1317 (2018).
29. Q. Xu, S. Qu, C. Ming, P. Qiu, q. yao, C. Zhu, T.-R. Wei, J. He, X. Shi, L. Chen, Conformal organic-inorganic semiconductor composites for flexible thermoelectrics. *Energ. Environ. Sci.* **13**, 511–518 (2020).
30. C. B. Vining, An inconvenient truth about thermoelectrics. *Nat. Mater.* **8**, 83–85 (2009).
31. M. Haras, T. Skotnicki, Thermoelectricity for IoT—A review. *Nano Energy* **54**, 461–476 (2018).
32. C. Geffroy, D. Lilley, P. S. Parez, R. Prasher, Techno-economic analysis of waste-heat conversion. *Joule* **5**, 3080–3096 (2021).
33. S. LeBlanc, S. K. Yee, M. L. Scullin, C. Dames, K. E. Goodson, Material and manufacturing cost considerations for thermoelectrics. *Renew. Sustain. Energy Rev.* **32**, 313–327 (2014).
34. R. R. Søndergaard, M. Hösel, N. Espinosa, M. Jørgensen, F. C. Krebs, Practical evaluation of organic polymer thermoelectrics by large-area R2R processing on flexible substrates. *Energy Sci. Eng.* **1**, 81–88 (2013).
35. K. Yazawa, A. Shakouri, Cost-efficiency trade-off and the design of thermoelectric power generators. *Environ. Sci. Technol.* **45**, 7548–7553 (2011).
36. G. Min, D. M. Rowe, Optimisation of thermoelectric module geometry for 'waste heat' electric power generation. *J. Power Sources* **38**, 253–259 (1992).
37. Y. Zhou, Z. Guo, J. He, Redesign high-performance flexible thermoelectrics: From mathematical algorithm to artificial cracks. *Appl. Phys. Lett.* **116**, 043904 (2020).
38. Y. Xing, R. Liu, J. Liao, C. Wang, Q. Zhang, Q. Song, X. Xia, T. Zhu, S. Bai, L. Chen, A device-to-material strategy guiding the "Double-high" thermoelectric module. *Joule* **4**, 2475–2483 (2020).
39. P. Qiu, T. Mao, Z. Huang, X. Xia, J. Liao, M. T. Agne, M. Gu, Q. Zhang, D. Ren, S. Bai, X. Shi, G. J. Snyder, L. Chen, High-efficiency and stable thermoelectric module based on liquid-like materials. *Joule* **3**, 1538–1548 (2019).
40. Q. Zhang, J. Liao, Y. Tang, M. Gu, C. Ming, P. Qiu, S. Bai, X. Shi, C. Uher, L. Chen, Realizing a thermoelectric conversion efficiency of 12% in bismuth telluride/skutterudite segmented modules through full-parameter optimization and energy-loss minimized integration. *Energ. Environ. Sci.* **10**, 956–963 (2017).
41. K. Nan, S. D. Kang, K. Li, K. J. Yu, F. Zhu, J. Wang, A. C. Dunn, C. Zhou, Z. Xie, M. T. Agne, H. Wang, H. Luan, Y. Zhang, Y. Huang, G. J. Snyder, J. A. Rogers, Compliant and stretchable thermoelectric coils for energy harvesting in miniature flexible devices. *Sci. Adv.* **4**, eaau5849 (2018).
42. S. J. Kim, J. H. We, B. J. Cho, A wearable thermoelectric generator fabricated on a glass fabric. *Energ. Environ. Sci.* **7**, 1959–1965 (2014).
43. F. Suarez, A. Nozariasbmarz, D. Vashaee, M. C. Öztürk, Designing thermoelectric generators for self-powered wearable electronics. *Energ. Environ. Sci.* **9**, 2099–2113 (2016).
44. P. Ying, H. Reith, K. Nielsch, R. He, Geometrical optimization and thermal-stability characterization of Te-free thermoelectric modules based on $MgAgSb/Mg_3(Bi,Sb)_2$. *Small* **18**, 2201183 (2022).
45. Q. Yang, S. Yang, P. Qiu, L. Peng, T.-R. Wei, Z. Zhang, X. Shi, L. Chen, Flexible thermoelectrics based on ductile semiconductors. *Science* **377**, 854–858 (2022).
46. S. K. Yee, S. LeBlanc, K. E. Goodson, C. Dames, $ per W metrics for thermoelectric power generation: Beyond *ZT*. *Energ. Environ. Sci.* **6**, 2561–2571 (2013).
47. O. I. Ibeagwu, Modelling and comprehensive analysis of TEGs with diverse variable leg geometry. *Energy* **180**, 90–106 (2019).
48. U. Erturun, K. Erermis, K. Mossi, Effect of various leg geometries on thermo-mechanical and power generation performance of thermoelectric devices. *Appl. Therm. Eng.* **73**, 128–141 (2014).
49. RMT Ltd., *Thermoelectric Power Generating Solutions* (RMT Ltd., 2018).
50. R. J. M. Vullers, R. van Schaijk, I. Doms, C. Van Hoof, R. Mertens, Micropower energy harvesting. *Solid-State Electron.* **53**, 684–693 (2009).
51. D. Beretta, N. Neophytou, J. M. Hodges, M. G. Kanatzidis, D. Narducci, M. Martin- Gonzalez, M. Beekman, B. Balke, G. Cerretti, W. Tremel, A. Zevalkink, A. I. Hofmann, C. Müller, B. Dörling, M. Campoy-Quiles, M. Caironi, Thermoelectrics: From history, a window to the future. *Mater. Sci. Eng. R Rep.* **138**, 100501 (2019).
52. W. He, D. Wang, H. Wu, Y. Xiao, Y. Zhang, D. He, Y. Feng, Y.-J. Hao, J.-F. Dong, R. Chetty, L. Hao, D. Chen, J. Qin, Q. Yang, X. Li, J.-M. Song, Y. Zhu, W. Xu, C. Niu, X. Li, G. Wang, C. Liu, M. Ohta, S. J. Pennycook, J. He, J.-F. Li, L.-D. Zhao, High thermoelectric performance in low-cost $SnS_{0.91}Se_{0.09}$ crystals. *Science* **365**, 1418–1424 (2019).
53. R. Dhawan, P. Madusanka, G. Hu, J. Debord, T. Tran, K. Maggio, H. Edwards, M. Lee, $Si_{0.97}Ge_{0.03}$ microelectronic thermoelectric generators with high power and voltage densities. *Nat. Commun.* **11**, 4362 (2020).
54. H. Wang, C. Yu, Organic thermoelectrics: Materials preparation, performance optimization, and device integration. *Joule* **3**, 53–80 (2019).
55. J. Cao, Y. Sim, X. Y. Tan, J. Zheng, S. W. Chien, N. Jia, K. Chen, Y. B. Tay, J.-F. Dong, L. Yang, H. K. Ng, H. Liu, C. K. I. Tan, G. Xie, Q. Zhu, Z. Li, G. Zhang, L. Hu, Y. Zheng, J. Xu, Q. Yan, X. J. Loh, N. Mathews, J. Wu, A. Suwardi, Upcycling silicon photovoltaic waste into thermoelectrics. *Adv. Mater.* **34**, e2110518 (2022).
56. O. H. Ando Junior, A. L. O. Maran, N. C. Henao, A review of the development and applications of thermoelectric microgenerators for energy harvesting. *Renew. Sustain. Energy Rev.* **91**, 376–393 (2018).
57. R. Yang, Y. Wang, T. Jin, Y. Feng, K. Tang, Development of a three-stage looped thermoacoustic electric generator capable of utilizing heat source below 120 C. *Energ. Conver. Manage.* **155**, 161–168 (2018).
58. M. Jaegle, Multiphysics simulation of thermoelectric systems-modeling of peltier cooling and thermoelectric generation. In: *Proceedings of the COMSOL Conference 2008 Hannover,* 22, (2008).
59. F. Scardulla, L. D'Acquisto, R. Colombarini, S. Hu, S. Pasta, D. Bellavia, A study on the effect of contact pressure during physical activity on photoplethysmographic heart rate measurements. *Sensors* **20**, 5052 (2020).
60. B. Zhu, X. Liu, Q. Wang, Y. Qiu, Z. Shu, Z. Guo, Y. Tong, J. Cui, M. Gu, J. He, Realizing record high performance in n-type Bi_2Te_3-based thermoelectric materials. *Energ. Environ. Sci.* **13**, 2106–2114 (2020).
61. G. J. Snyder, A. H. Snyder, Figure of merit *ZT* of a thermoelectric device defined from materials properties. *Energ. Environ. Sci.* **10**, 2280–2283 (2017).
62. B. N. Taylor, C. E. Kuyatt, *Guidelines for Evaluating and Expressing the Uncertainty of NIST Measurement Results* (U.S. Department of Commerce, Technology Administration, National Institute of Standards and Technology, 1994), vol. 1297.
63. D. K. Schroder, Contact resistance and Schottky barriers, in *Semiconductor Material and Device Characterization* (John Wiley & Sons Inc., ed. 3, 2005), chap. 3, pp. 138–149.
64. Y. Wang, Y. Shi, D. Mei, Z. Chen, Wearable thermoelectric generator to harvest body heat for powering a miniaturized accelerometer. *Appl. Energy* **215**, 690–698 (2018).
65. D.-W. Ao, W.-D. Liu, Z.-H. Zheng, X.-L. Shi, M. Wei, Y.-M. Zhong, M. Li, G.-X. Liang, P. Fan, Z.-G. Chen, Assembly-free fabrication of high-performance flexible inorganic thin-film thermoelectric device prepared by a thermal diffusion. *Adv. Energ. Mater.* **12**, 2202731 (2022).
66. M. Wei, X.-L. Shi, Z.-H. Zheng, F. Li, W.-D. Liu, L.-P. Xiang, Y.-S. Xie, Y.-X. Chen, J.-Y. Duan, H.-L. Ma, G.-X. Liang, X.-H. Zhang, P. Fan, Z.-G. Chen, Directional thermal diffusion realizing inorganic Sb_2Te_3/Te hybrid thin films with high thermoelectric performance and flexibility. *Adv. Funct. Mater.* **32**, 2207903 (2022).

Acknowledgments

Funding: This research was supported by the National Natural Science Foundation of China (grant nos. 11934007 and 11874194), the leading talents of the Guangdong Province Program (grant no. 00201517), the Financial Support for Outstanding Talents Training Fund in Shenzhen (grant no. 202108), the Science and Technology Innovation Committee Foundation of Shenzhen (grant nos. RCBS20200714114959040, JCYJ20200109141205978, JCYJ20190809145205497, and ZDSYS20141118160434515), the Guangdong-Hong Kong-Macao Joint Laboratory (grant no. 2019B121205001). G.W.H. acknowledges the support by A*STAR under its 2019 AME IRG and YIRG Grant Calls (grant no. A2083c0059), and the NRF Central Gap Fund (grant nos. NRF2020NRF-CG001-023 and NUS TAP25002021-01-01). **Author contributions:** Y.Z. and J.H. conceived the idea and designed the experiments. J.H. and G.W.H. supervised the project. Y.Z. contributed to the device modeling, fabrication, and characterization. Y.Z. and X.L. contributed to the industrial techno-economic analysis. Y.Z., B.J., T.D., D.M., and T.W. contributed to the material characterizations. Y.Z., G.W.H., and J.H. contributed to the writing, and all authors revised the manuscript. **Competing interests:** The authors declare that they have no competing interests. **Data and materials availability:** All data needed to evaluate the conclusions in the paper are present in the paper and/or the Supplementary Materials.

Submitted 31 October 2022
Accepted 12 December 2022
Published 13 January 2023
10.1126/sciadv.adf5701